Research Square

Preprints are preliminary reports that have not undergone peer review.
They should not be considered conclusive, used to inform clinical practice,
or referenced by the media as validated information.

Optimization of a radio-frequency inductively coupled plasma thruster

Lucas Andrin
Ecole Polytechnique
Trevor Lafleur
t.lafleur@unsw.edu.au
UNSW Canberra

Research Article

Keywords: Inductively coupled plasma, radio-frequency, electrothermal thruster, optimization, impedance matching network

Posted Date: November 12th, 2026

DOI: https://doi.org/10.21203/rs.3.rs-11493330/v1

License: This work is licensed under a Creative Commons Attribution 4.0 International License.
Read Full License

Additional Declarations: No competing interests reported.

Optimization of a radio-frequency inductively coupled plasma thruster

Lucas Andrin[1] and Trevor Lafleur[2*]

[1]Ecole Polytechnique, Palaiseau, F-91128, France.
[2]School of Engineering and Technology, University of New South Wales, Northcott Drive, Canberra, 2612, ACT, Australia.

*Corresponding author(s). E-mail(s): t.lafleur@unsw.edu.au;

Abstract

Radio-Frequency (RF) Inductively Coupled Plasma (ICP) thrusters are an emerging electrothermal propulsion technology that creates a high-density plasma to heat propellant which is then accelerated through a converging-diverging nozzle. Using a multi-physics model accounting for plasma production, plasma-coil electromagnetic coupling, heat transfer, and impedance matching, this work investigates optimization of a complete RF ICP propulsion system for small satellite missions by varying important design and operating parameters including thruster size, propellant type, mass flow rate, and RF frequency. Aside from thruster performance, an important optimization metric is minimization of the total propulsion system mass, and for a representative small satellite mission power and total impulse of 100 W and 1 kNs respectively, xenon is found to be an attractive propellant because of its low ionization threshold, high atomic mass, and high storage density. This not only reduces propulsion system inert mass, but also yields a thrust-to-power ratio almost ten times higher than other electric propulsion technologies such as gridded ion or Hall thrusters.

Keywords: Inductively coupled plasma, radio-frequency, electrothermal thruster, optimization, impedance matching network

1 Introduction

An electrothermal thruster is an electric propulsion system that uses electrical power from a spacecraft to heat propellant which is then expanded and accelerated through

a nozzle to generate thrust. Typical examples of electrothermal thrusters include arcjets and resistojets. Arcjets create an electrical arc between two electrodes that is used to heat propellant gas. Although very high temperatures can be achieved (as high as 10,000-20,000 K), the immersed electrodes can experience serious erosion and vaporization which reduces thruster life [1]. Resistojets avoid this problem by simply heating propellant via a physical heating element. However, material thermal considerations limit the maximum achievable temperature and, as a consequence, the maximum specific impulse[2].

Microwave Electrothermal Thrusters (METs) are an alternative electrothermal propulsion technology that aims to overcome the shortcomings of arcjets and resistojets. Here, microwaves are injected into a chamber, and if the chamber geometry is carefully matched to the microwave frequency, the microwave electric field can be amplified and becomes high enough to ignite a plasma. This plasma then heats the remaining propellant gas via various collisional processes. Thus, propellant heating occurs without any physical elements or immersed electrodes [3]. An important drawback of METs however, is that they require high frequencies (typically of the order of a few GHz), which has implications on the maximum electrical efficiency of the thruster power generator [4]. Moreover, as METs are resonant devices, the size and geometry of the chamber must be matched to the chosen frequency with a high level of precision. Studies have been conducted on METs using various propellants such as simulated hydrazine, ammonia, nitrogen, and water [5] [6]. In 2023, the US company Momentus successfully tested the MET for the first time in space on the Vigoride spacecraft using water propellant [6].

Another type of electrodeless electrothermal propulsion systems is a Radio-Frequency (RF) Inductively Coupled Plasma (ICP) thruster. Here, an RF coil is wrapped around the outside of a dielectric chamber and power is coupled to the plasma via the inductive electric field. This plasma then heats the remaining propellant gas through collisions and the hot gas is then accelerated through a nozzle to generate thrust. An important advantage of this system is that the required RF frequency is only in the MHz range, and as the device is non-resonant, there is more flexibility in frequency selection. ICPs are also widely used for many different industrial applications such as plasma spraying, cutting, and material processing. The idea of using plasma torches for space propulsion first appeared in the 1960's with serious experiments conducted in the early 1990's and late 2000's [7, 8].

While ICP thrusters were first proposed in 1960's, it is only in the last 5-10 years that dedicated modeling efforts have been undertaken to better understand the underlying system operation and relevant scaling laws. For example, Fujino and Yamauchi [9] developed a 2D fluid simulation that modeled the heating of the gas, the coupling between the plasma and the RF coil, and supersonic expansion through the nozzle. Shortly after, Lafleur & Corr [10] developed an analytical discharge model and characterized an experimental ICP thruster using argon propellant. In 2025, Sadler *et al.* [11] developed a 3D model coupling Computational Fluid Dynamics (CFD) with electrodynamics to simulate the behavior of the plasma inside the thruster, and to better understand the impact of the gas injection system on system performance. They managed to reach a precision between 4 and 25% when comparing their predictions to available data.

The above papers only considered argon, and were developed to model existing experimental devices which were noted to be far from optimal in terms of performance. The present work aims to expand and improve these previous modeling efforts by providing a more complete description of RF ICP thrusters to better identify important scaling laws. To do this, the original analytical model of Lafleur and Corr (previously validated in Refs. [10] and [12]) is enhanced by removing several important assumptions, considering several different propellants, and by including additional models not only for the thruster, but also the electrical system and propellant storage tank. This improved model is then used to study the optimization of RF ICP thrusters by varying the propellant type, thruster dimensions, mass flow rate, and RF frequency.

2 Theoretical model of the ICP thruster

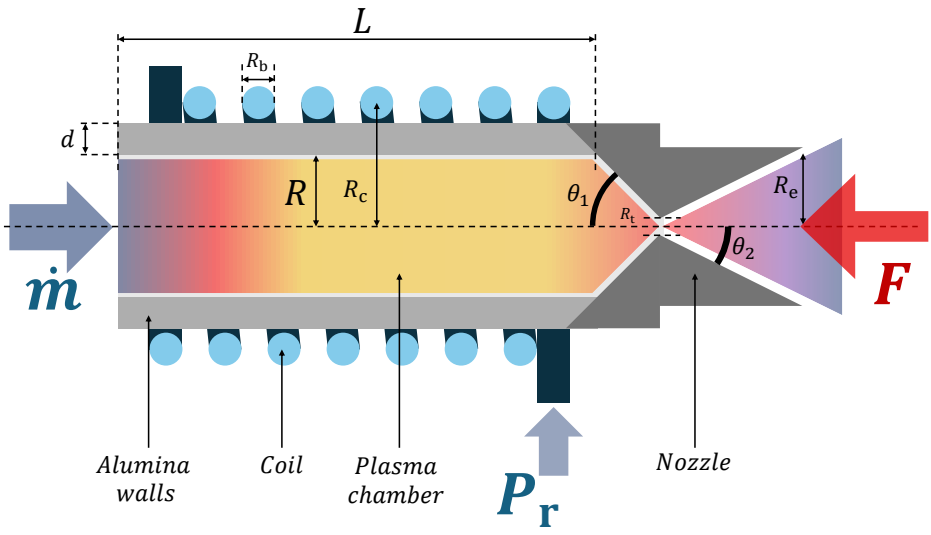


Fig. 1 Schematic of an RF ICP thruster.

Figure 1 illustrates the basic operation of an RF ICP thruster. A given mass flow rate, $\dot{m}$, enters the plasma chamber, while an electrical power P_{rf} is applied to a coil wrapped around the outside. The inductive electric field from the coil enables a high-density, partially ionized, plasma to be created. Various collisional process, such as electron-neutral elastic scattering, then transfer power from the plasma to the remaining un-ionized propellant leading to strong gas heating. This hot gas is then expanded and accelerated through a physical rocket nozzle to generate a thrust, F.

The main geometric parameters of the thruster are indicated in Fig. 1 and summarized in Tab. 1. Here, R and L are the plasma chamber radius and length respectively, and are unknowns to be determined as a result of the optimization process. The lower

Table 1 Thruster geometric parameters.

Symbol	Definition	Value
R	Chamber radius	> 6 mm
L	Chamber length	> 50 mm
d	Wall thickness	4 mm
R_t	Throat radius	1 mm
R_e	Exit radius	10 mm
R_b	Coil wire radius	1.5 mm
R_c	Coil radial location	$R + 5.5$ mm
L_c	Coil axial extent	$\sim 0.9L$
N	Number of turns	7
θ_1	Converging angle	45°
θ_2	Diverging angle	26.5°

limit values for R and L in Tab. 1 will be explained further in the optimization section. The choice for the coil axial extent, L_c, is a compromise. On the one hand, if the coil is too short, electrical power may be poorly transmitted to the plasma at the edges of the chamber, and the coil turns may touch or get too close to each other. But on the other hand, if L_c is too close to L, the coil may touch the nearby nozzle and gas injection system, resulting in possible arcing. In the subsections below, different physics models are described linking the thruster performance to various inputs such as $\dot{m}$ and P_rf.

2.1 Compressible flow

Assuming isentropic flow, and for a given stagnation pressure, p_s, inside the chamber, the gas flow in the nozzle will go supersonic downstream of the throat if the following criteria is satisfied:

$$p_\mathrm{e} < p_\mathrm{s} \left(\frac{2}{\gamma + 1} \right)^{\frac{\gamma}{\gamma - 1}} \tag{1}$$

where p_e is the static pressure at the nozzle exit and γ is the ratio of specific heats. For the noble gases and temperatures considered in this work, $\gamma \approx 1.67$, which implies that $p_\mathrm{exit}/p_\mathrm{s} < 0.49$. Assuming that the flow goes sonic at the nozzle throat, the mass flow rate is choked and given by

$$\dot{m} = \frac{p_\mathrm{s} \gamma A_\mathrm{t}}{\sqrt{\frac{\gamma k_\mathrm{B} T_\mathrm{s}}{M}}} \sqrt{\left(\frac{2}{\gamma + 1} \right)^{\frac{\gamma + 1}{\gamma - 1}}} \tag{2}$$

with $A_\mathrm{t} = \pi R_\mathrm{t}^2$ the nozzle throat cross-sectional area, R_t the nozzle throat radius, M the gas atomic/molecular mass, k_B Boltzmann's constant, and T_s the stagnation temperature. The ideal gas law then links the stagnation parameters to the neutral gas density, n_g, in the chamber

$$p_\mathrm{s} = n_\mathrm{g} k_\mathrm{B} T_\mathrm{s} \tag{3}$$

Once T_s is known, the nozzle exit velocity and thruster performance can be deduced from the following equations

$$v_e = \sqrt{\frac{2\gamma}{\gamma-1}\frac{k_\mathrm{B}T_\mathrm{s}}{M}\left[1-\left(\frac{p_\mathrm{e}}{p_\mathrm{s}}\right)^{\frac{\gamma-1}{\gamma}}\right]} \tag{4}$$

$$\frac{A_\mathrm{t}}{A_\mathrm{e}} = \left(\frac{\gamma+1}{2}\right)^{\frac{1}{\gamma-1}}\left(\frac{p_\mathrm{e}}{p_\mathrm{s}}\right)^{\frac{1}{\gamma}}\sqrt{\frac{\gamma+1}{\gamma-1}\left[1-\left(\frac{p_\mathrm{e}}{p_\mathrm{s}}\right)^{\frac{\gamma-1}{\gamma}}\right]} \tag{5}$$

$$F = f_\theta \dot{m} v_\mathrm{e} + p_\mathrm{e}A_\mathrm{e} \tag{6}$$

$$I_\mathrm{sp} = \frac{F}{\dot{m}g_0} \tag{7}$$

$$\eta_\mathrm{T} = \frac{F^2}{2\dot{m}P_\mathrm{in}} \tag{8}$$

Here v_e is the nozzle exit velocity, $f_\theta = \frac{1}{2}(1+\cos\theta_2)$ is a thrust correction factor accounting for nozzle divergence, A_e is the cross-sectional area of the nozzle exit, I_sp is the specific impulse, g_0 is the sea-level gravitational acceleration of the Earth, η_T is the thruster efficiency, and $P_\mathrm{in} = P_\mathrm{rf} + \dot{m}c_\mathrm{p}T_\mathrm{in}$ is the total input power, which depends on the RF input power P_rf, the inlet temperature T_in, and the specific heat at constant pressure, c_p.

2.2 Gas power balance

At steady-state, enthalpy flow through the thruster, conductive heat loss to the thruster walls ($P_\mathrm{w,cond}$), and heating due to electron collisions (P_col), must balance

$$\dot{m}c_\mathrm{p}(T_\mathrm{s}-T_\mathrm{in}) + P_\mathrm{w,cond} = P_\mathrm{col} \tag{9}$$

Radiative heat losses will be separately considered below. For a cylindrical thruster chamber, $P_\mathrm{w,cond}$ can be written as follows [10]:

$$P_\mathrm{w,cond} = 4\chi_{01}\mathrm{J}_1(\chi_{01})\kappa(T_0-T_\mathrm{w})L\left(1+\frac{\pi^2R^2}{\chi_{01}^2L^2}\right) \tag{10}$$

where χ_{01} is the first root of the zeroth-order Bessel function of the first kind, J_0, J_1 the first-order Bessel function of the first kind, T_0 is the maximum gas temperature inside the chamber, T_w is the chamber wall temperature, and $\kappa \sim \kappa(T_0)$ is the thermal conductivity of the gas (see Appendix B). The maximum and stagnation temperatures are related according to the following equation [10]

$$T_\mathrm{s} - T_\mathrm{w} = \frac{2\mathrm{J}_1(\chi_{01})}{\chi_{01}}(T_0-T_\mathrm{w}) \tag{11}$$

The wall temperature is not known beforehand and can vary with input conditions. Ignoring thermal conduction to the spacecraft, the wall temperature is determined from a thermal balance of the thruster chamber

$$P_{\mathrm{w,cond}} = P_{\mathrm{w,rad}} - P_{\mathrm{sat,rad}} \tag{12}$$

Here $P_{\mathrm{w,rad}} = S\sigma_{\mathrm{SB}}T_{\mathrm{w}}^4$ is the power radiated by the outer chamber walls towards the rest of the spacecraft with S the total surface area of the chamber walls, and $P_{\mathrm{sat,rad}} = S\sigma_{\mathrm{SB}}T_{\mathrm{sat}}^4$ represents radiative heat transfer from the spacecraft to the thruster with $T_{\mathrm{sat}} = 300$ K an assumed spacecraft reference temperature. As the thruster chamber is made of a dielectric material (such as alumina), we have assumed an emissivity approximately equal 1.

The above equations enable us to link T_{s} and P_{col}, and to determine T_{w} and T_0 in the process. However, we still need to link P_{col} to the input electrical power, which requires knowledge of the plasmas properties inside the chamber.

2.3 Plasma power balance

Considering steady-state where the neutral (n_{g}) and electron (n_e) densities are constant, ionization balance requires

$$(2h_{\mathrm{L}}A_{\mathrm{L}} + h_{\mathrm{T}}A_{\mathrm{T}})u_{\mathrm{B}} = n_{\mathrm{g}}K_{\mathrm{iz}}V \tag{13}$$

Here $V = \pi R^2 L$ is the volume of the thruster chamber, $A_{\mathrm{L}} = \pi R^2$ is the chamber cross-sectional area, $A_{\mathrm{T}} = 2\pi RL$ is the lateral surface area, h_{L} and h_{R} are axial and radial sheath edge-to-center density ratios (which account for plasma transport; see below), $u_{\mathrm{B}} = \sqrt{k_{\mathrm{B}}T_{\mathrm{e}}/M}$ is the Bohm velocity with T_{e} the electron temperature, and K_{iz} is the ionization rate coefficient. The left-hand side of Eqn. 13 represents plasma loss to the walls, while the right-hand side represents plasma production due to ionization. The sheath edge-to-center density ratios, h_{L} and h_{R} are found using the empirical relations below

$$h_{\mathrm{L}} \approx 0.86\left[3 + \frac{1}{2}\frac{L}{\lambda_{\mathrm{i}}} + \frac{1}{5}\frac{T_{\mathrm{i}}}{T_{\mathrm{e}}}\left(\frac{L}{\lambda_{\mathrm{i}}}\right)^2\right]^{-1/2} \tag{14}$$

$$h_{\mathrm{R}} \approx 0.8\left[4 + \frac{R}{\lambda_{\mathrm{i}}} + \frac{T_{\mathrm{i}}}{T_{\mathrm{e}}}\left(\frac{R}{\lambda_{\mathrm{i}}}\right)^2\right]^{-1/2} \tag{15}$$

where $T_{\mathrm{i}} \approx T_{\mathrm{s}}$ is the ion temperature, and $\lambda_{\mathrm{i}} = 1/(\sigma_{\mathrm{i}}n_{\mathrm{g}})$ is the ion-neutral mean free path with $\sigma_{\mathrm{i}} \approx 10^{-18}$ m^2 the ion-neutral collision cross-section [13]. The electron-neutral collisional processes considered include ionization, excitation, and elastic scattering, which lead to power losses given by

$$P_{\mathrm{iz}} = \varepsilon_{\mathrm{iz}}K_{\mathrm{iz}}n_{\mathrm{e}}n_{\mathrm{g}}V \tag{16}$$

$$P_{\mathrm{exc}} = \left(\sum_i \varepsilon_{\mathrm{exc},i}K_{\mathrm{exc},i}\right)n_{\mathrm{e}}n_{\mathrm{g}}V \tag{17}$$

$$P_{\mathrm{col}} = \frac{3m}{M}k_{\mathrm{B}}(T_{\mathrm{e}} - T_{\mathrm{s}})K_{\mathrm{el}}n_{\mathrm{e}}n_{\mathrm{g}}V \tag{18}$$

Here K_{iz}, $\varepsilon_{\mathrm{iz}}$, and P_{iz} are the ionization rate coefficient, threshold energy, and power loss respectively, P_{exc} is the excitation power loss, $K_{\mathrm{exc},i}$ and $\varepsilon_{\mathrm{exc},i}$ are the

excitation rate coefficient and threshold energy for excitation process i, K_{el} is the elastic scattering rate coefficient, and m is the electron mass. The total power absorbed by the plasma, P_{abs}, is equal to the sum of all collisional power losses above, as well as the plasma kinetic power loss to the walls. This can be written as

$$P_{\mathrm{abs}} = n_{\mathrm{e}} u_{\mathrm{B}} (2h_{\mathrm{L}} A_{\mathrm{L}} + h_{\mathrm{R}} A_{\mathrm{T}}) \varepsilon_{\mathrm{T}} \tag{19}$$

where

$$\varepsilon_{\mathrm{T}} = \varepsilon_{\mathrm{c}} + \frac{k_{\mathrm{B}} T_{\mathrm{e}}}{2} \left[5 + \ln \left(\frac{M}{2\pi m} \right) \right] \tag{20}$$

and the effective collisional energy loss per electron-ion pair produced from ionization is

$$\varepsilon_{\mathrm{c}} = \varepsilon_{\mathrm{iz}} + \sum_i \varepsilon_{\mathrm{exc},i} \frac{K_{\mathrm{exc},i}}{K_{\mathrm{iz}}} + \frac{3m}{M} k_{\mathrm{B}} (T_{\mathrm{e}} - T_{\mathrm{s}}) \frac{K_{\mathrm{el}}}{K_{\mathrm{iz}}} \tag{21}$$

All rate coefficients depend on the electron temperature, and assuming a Maxwellian electron distribution function, are calculated using the following formula [13]

$$K = \frac{\bar{v}_{\mathrm{e}}}{T_{\mathrm{e}}^2} \int_0^\infty \sigma(\varepsilon) \varepsilon \exp \left(-\frac{\varepsilon}{T_{\mathrm{e}}} \right) \mathrm{d}\varepsilon \tag{22}$$

In this equation, $\bar{v}_{\mathrm{e}}$ is the electron thermal speed, and both ε and T_{e} are in units of eV. The rate coefficients determined from Eqn. 22 are provided in Appendix A for all collisional processes considered.

2.4 RF power and impedance matching network

Because of the intrinsic resistance of the RF coil, not all of the input power is absorbed by the plasma. Defining the resistance of the coil without plasma as r_{coil}, and the resistance with plasma as r_{p}, the absorbed power can be written as

$$P_{\mathrm{abs}} = \eta_{\mathrm{rf}} P_{\mathrm{rf}} \tag{23}$$

$$\eta_{\mathrm{rf}} = \frac{r_{\mathrm{p}}}{r_{\mathrm{p}} + r_{\mathrm{coil}}} \tag{24}$$

where η_{rf} is the RF power transfer efficiency. The intrinsic resistance depends on the frequency and geometry of the coil[14], and can be estimated using the following equations where the electromagnetic skin depth is used to evaluate an effective cross-section for current flow in the coil wire

$$r_{\mathrm{coil}} = \frac{\alpha_{\mathrm{r}} L_{\mathrm{tot}}}{2R_{\mathrm{b}}} \sqrt{\frac{\mu_0 f \rho_{\mathrm{el}}}{\pi}} \tag{25}$$

$$L_{\mathrm{tot}} = L_0 + 2N\pi R_{\mathrm{c}} \sqrt{1 + \left(\frac{L_{\mathrm{c}}}{2\pi N R_{\mathrm{c}}} \right)^2} \tag{26}$$

Here L_{tot} is the total length of the coil wire, f is the RF frequency, ρ_{el} is the resistivity of the wire material (assumed here to be copper for which $\rho_{\mathrm{el}} \approx 1.68 \times 10^{-8}$

Ω m), R_c is the radius of the coil, L_c is the axial extent of the coil, N is the number of turns, and L_0 is the "dead" length of the coil (used to connect it to the impedance matching network, and assumed to be ~ 10 cm for each coil leg). The coefficient α_r accounts for several factors [14]. For example, the actual resistance of the coil can be much higher than that determined from the above equations because of the *proximity effect*. Essentially, as the coil turns are relatively close to each other, the radial current profile inside each wire can become distorted and the effective cross-sectional area for current flow is reduced. The proximity effect is difficult to accurately quantify, but typically increases the resistance by a factor of between 2-4. Here, we assume a mid-range value giving $\alpha_r = 3$.

The plasma resistance, r_p, is determined from the following equations [**?**]

$$\frac{r_p}{r_{coil}} = 2Q\left(\frac{R}{R_c}\right)^2 \mathrm{Re}\left[\frac{\mathrm{i}J_1(kR)}{kRJ_0(kR)}\right] \tag{27}$$

$$k = \frac{\omega\sqrt{\epsilon_p}}{c} \tag{28}$$

$$\epsilon_p = 1 - \frac{\omega_{pe}^2}{\omega(\omega - \mathrm{i}\nu_m)} \tag{29}$$

where $\omega_{pe} = \sqrt{e^2 n_e/(\epsilon_0 m)}$ is the electron plasma frequency, $\nu_m \approx n_g(K_{iz} + \sum_i K_{exc,i} + K_{el})$ is the electron momentum transfer collision frequency, k is a complex wavenumber, c is the speed of light, ϵ_0 the permittivity of free space, $\omega = 2\pi f$ is the angular frequency, ϵ_p is a relative complex plasma permittivity, and $Q = \omega l_{coil}/r_{coil}$ is the unloaded Q-factor of the coil with $l_{coil} = \mu_0 N^2 R_c^2/L_c$ the coil inductance and μ_0 the permeability of free space.

Although we now have a complete set of equations that give all characteristics of the thruster for a given mass flow rate and RF power, we cannot in general directly control P_{rf}. This is because there may be reflected power depending on the mismatch between the equivalent electrical load of the thruster, and the output impedance of the RF generator. To minimize or eliminate the reflected power, an Impedance Matching Network (IMN) is needed [15], as indicated in Fig. 2.

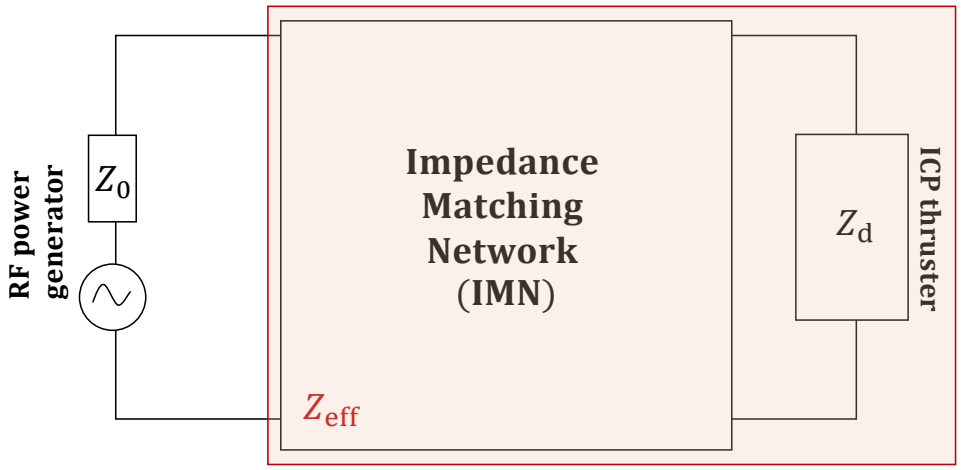


Fig. 2 Electrical schematic of the thruster.

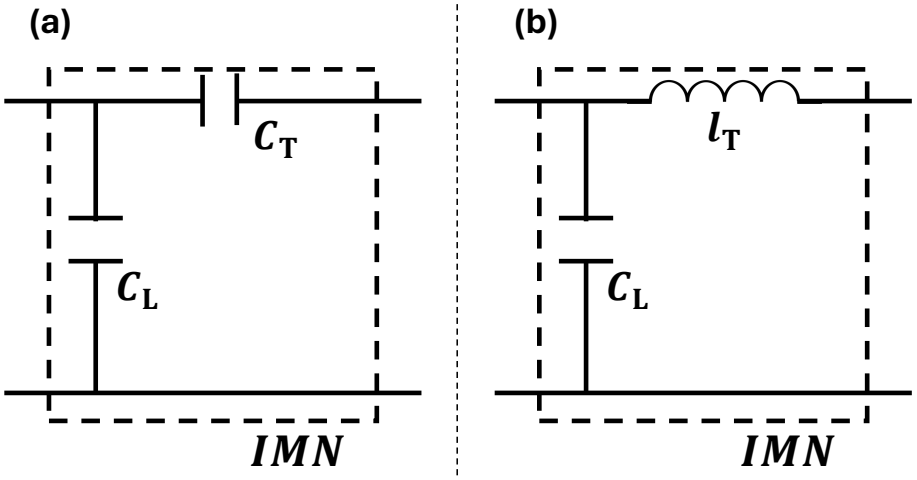


Fig. 3 Schematic of two L-type IMNs. **(a)** double C type, **(b)** L+C type.

Several configurations can be used for the IMN, but in this work, we consider an L-type network (see Fig. 3). The L-type network in Fig. 3 (a) will be called a "double

C" IMN and consists of two capacitors C_T and C_L. With the correct capacitor values, one can ensure that $Z_\mathrm{eff} = Z_0$ where Z_0 is the output impedance of the RF generator. In this case, $P_\mathrm{rf} = P_\mathrm{gen}$ with P_gen the forward power from the generator, and there is no reflected power. The required capacitor values can be determined from [13]

$$C_\mathrm{L} = \frac{1}{\omega}\sqrt{\frac{1}{r_\mathrm{d} Z_0} - \frac{1}{Z_0^2}} \tag{30}$$

$$C_\mathrm{T} = \frac{1}{\omega\left(X_\mathrm{d} - \sqrt{r_\mathrm{d} Z_0 - r_\mathrm{d}^2}\right)} \tag{31}$$

where $r_\mathrm{d} = r_\mathrm{p} + r_\mathrm{coil}$ is the combined resistance of the thruster and coil, and X_d is the equivalent reactance of the coil and plasma given by

$$\frac{X_\mathrm{d}}{r_\mathrm{coil}} = Q\left\{\left(1 - \frac{R^2}{R_\mathrm{c}^2}\right) + 2\left(\frac{R}{R_\mathrm{c}}\right)^2 \mathrm{Im}\left[\frac{\mathrm{i}\mathrm{J}_1(kR)}{kR\mathrm{J}_0(kR)}\right]\right\} \tag{32}$$

From careful observation of Eqns. 30 and 31, it can be seen that for some discharge conditions, C_T may become negative. Thus, perfect matching can no longer be achieved with a "double C" IMN, and C_T must be replaced with an inductor leading to the second L-type network in Fig. 3 (b) which we will refer to as an "L+C" IMN. In this case, the required inductance, l_T, becomes

$$l_\mathrm{T} = \frac{\sqrt{r_\mathrm{d} Z_0 - r_\mathrm{d}^2} - X_\mathrm{d}}{\omega} \tag{33}$$

For some conditions (such as low frequencies), the use of l_T again allows perfect matching. However, while the equivalent series resistance of many capacitors is very low (such that they can often be assumed to be lossless), the inductor has a much higher resistance resulting in power losses in addition to those from the coil itself.

For the following sections, we need to link the resistance, r_IMN, of the IMN coil to its inductance l_T. The resistance of the coil is proportional to the total length of the coil wire, and the square root of the frequency. The total length of the coil wire is proportional to its number of turns N_IMN and radius R_IMN. Because, $l_\mathrm{T} \propto N_\mathrm{IMN}^2 R_\mathrm{IMN}^2$, we can thus assume that $r_\mathrm{IMN} \propto \sqrt{l_\mathrm{T}}\sqrt{f}$. This will be used for the optimization section. The reference data of $r_\mathrm{IMN} = 2$ mΩ for $l_\mathrm{T} = 10$ nH and $f = 2$ MHz gives the following scaling

$$r_\mathrm{IMN} = 2\mathrm{m}\Omega\sqrt{\frac{l_\mathrm{T}}{10\mathrm{nH}}}\sqrt{\frac{f}{2\mathrm{MHz}}} \tag{34}$$

The IMN power efficiency then becomes

$$\eta_\mathrm{IMN} = \frac{P_\mathrm{rf}}{P_\mathrm{gen}} = \frac{r_\mathrm{p} + r_\mathrm{coil}}{r_\mathrm{p} + r_\mathrm{coil} + r_\mathrm{IMN}} \tag{35}$$

Combined with η_rf, η_IMN links the power absorbed by the plasma to the power delivered by the generator.

Lastly, we need to address the link between the generator power, P_gen, and the incoming DC power from the satellite, P_sat. The generator (or any separate power

processing unit) needs to transform this DC power into RF power that is usable by the thruster. The conversion efficiency is difficult to accurately estimate and typically varies with frequency. The generator efficiency, η_g, typically decreases when increasing frequency [4], with typical maximum efficiencies of about 90% having been achieved with actual flight-qualified ICP systems [16]. For the purpose of the optimization work below, since we do not have any precise experimental data regarding $\eta_g(f)$, we will assume constant $\eta_g = 90\%$ for any frequency.

2.5 Propulsion system mass and volume

The total mass and volume of the propulsion system are important factors, particularly for small satellite missions. Not only is minimization of the mass and volume relevant to system optimization, but as highlighted in several other works [17], these factors can help provide more "universal" metrics to aid with propulsion system technology trade studies and propellant selection.

The total mass M_{tot} of the propulsion system is composed of the inert mass M_{dry} (mass of the system without its propellant) and the propellant mass M_p. The inert mass is in turn composed of the thruster mass M_{th}(which includes the chamber, nozzle, RF generator, etc.) and the mass of the propellant storage tank M_{tank}.

In the present work, we consider the optimization of an RF ICP thruster within the context of a small satellite mission. For this mission, the total satellite mass is set to 20 kg and the required Δv is 50 m/s. Therefore, the total impulse that the propulsion system must provide is approximately $I_T = 1$ kN s. We then consider each operating condition (i.e. P_{rf} and $\dot{m}$) as if it were a possible nominal condition of the thruster. That is to say, as if the thruster was meant to be operated at those values. Once the nozzle exit velocity and specific impulse are known, the rocket equation can then be used to determine the required propellant mass. Based on chosen storage conditions, the mass density of the propellant, ρ_p, is then established, from which the required propellant volume, V_p, can be determined. Thus, the propellant mass and volume are obtained from

$$M_p = \frac{I_T}{I_{sp} g_0} \tag{36}$$

$$V_p = \frac{M_p}{\rho_p} \tag{37}$$

The volume of the tank V_{tank} is usually slightly higher than that of the propellant, due to multiple factors [18–20], such as the need to account for any residual propellant stuck inside the tank and flow distribution system, any internal tank structures (such as bladders or barriers to prevent sloshing), and ullage to account for tank-propellant thermal expansion. Here, we will assume that the tank volume is therefore approximately 10% larger than the propellant volume.

Assuming a cylindrical tank (with spherical ends) pressurized to a storage pressure of p_{tank}, the tank mass can be estimated from

$$M_{tank} = \frac{6\alpha_{sf}\alpha_{st}\rho_{tank}p_{tank}V_{tank}}{\sigma_{tank}}\left(\frac{1+2\beta}{4+3\beta}\right) \tag{38}$$

where $\beta = R_{\text{tank}}/L_{\text{tank}}$ is the ratio of the tank radius and length, ρ_{tank} is the tank material mass density, and σ_{tank} the ultimate tensile strength of the tank material. Assuming titanium, we will use $\rho_{\text{tank}} = 4,430$ kg/m^3 and $\sigma_{\text{tank}} = 880$ MPa. In Eqn. 38, α_{st} is a stress concentration factor, and α_{sf} is a safety factor, set here to 2.5 and 2 respectively.

The dry mass of the thruster can be estimated from the mass-to-power ratio obtained from existing electrothermal thrusters, which is typically of the order of 5 kg/kW [21, 22]. Since the target satellite mass considered here is $P_{\text{sat}} = 100$ W, this implies that $M_{\text{dry}} \sim 500$ g. The total mass of the propulsion system is then $M_{\text{tot}} = M_{\text{th}} + M_{\text{tank}} + M_{\text{p}}$.

3 Thruster optimization for fixed geometry and RF frequency

In this section, we solve the thruster model by varying $\dot{m}$ and P_{rf} for a fixed geometry with $R = 0.95$ cm and $L = 6.0$ cm (representative of the plasma source in Ref. [10]), and a fixed frequency of $f = 13.56$ MHz. This is done for the three noble gas propellants argon, krypton, and xenon. While many possible propellant options are available, experimental data already exists for argon [9, 10, 12], and previous studies have demonstrated that xenon and krypton give the highest thrust-to-power ratio [17, 23]: an attractive feature for small satellites which are power limited. Table 2 summarizes several key properties of these gases where ρ_{storage} is the mass density at a representative storage temperature and pressure of $T_{\text{storage}} = T_{in} = 300$ K and $p_{\text{storage}} = 200$ bar respectively.

While each propellant type has many different electron impact excitation levels that are possible (each with their own threshold energy, $\varepsilon_{\text{exc},j}$ and rate coefficient, $K_{\text{exc},j}$), here for simplicity we consider a smaller number of effective lumped levels [24], as indicated in Tab. 3. Appendix A details the different rate coefficients, and the way they are implemented in the model.

Figure 4 shows the N2 chart of the thruster, and the link between every model element. Given the chosen inputs, the main task is solving for the plasma/gas properties within the thruster (red region). Once this is done, thruster performance can then be evaluated.

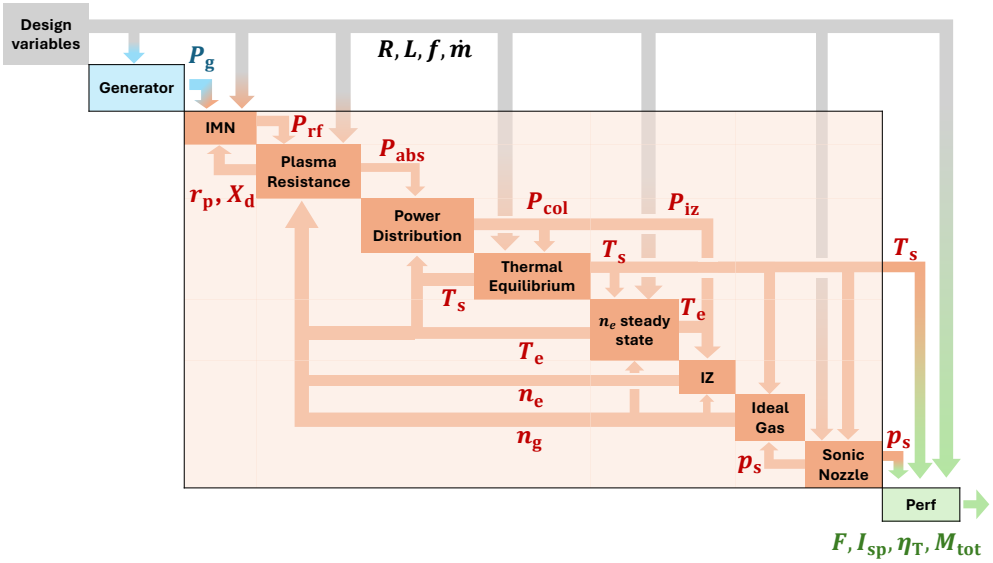


Fig. 4 N2 chart of the RF ICP thruster.

Table 2 Properties of argon, krypton, and xenon. The storage temperature and pressure for all three propellants is $T_{\text{storage}} = 300$ K and $p_{\text{storage}} = 200$ bar respectively.

	Ar	Kr	Xe
M (u)	39.948	83.798	131.293
c_p (J/K/kg)	520	248	158
ε_{iz} (eV)	15.76	14.00	12.13
ρ_{storage} (kg/m^3)	335.84	916.14	2093.7

Table 3 Effective lumped excitation levels for argon, krypton, and xenon.

	Ar	Kr	Xe
$\varepsilon_{\text{exc},1}$ (eV)	11.55	9.915	8.315
$\varepsilon_{\text{exc},2}$ (eV)	13.00	11.30	9.447
$\varepsilon_{\text{exc},3}$ (eV)	14.00	11.998	9.917
$\varepsilon_{\text{exc},4}$ (eV)		12.75	11.7

3.1 Fixed mass flow rate

Because of the structure of the model equations, a simple solution approach is to treat the stagnation temperature, T_s, as an "input". By then fixing $\dot{m}$, the required power is determined as an "output", and which presents the power needed to achieve

the stagnation temperature originally selected. The specific solution process is then as follows. For a given T_s and $\dot{m}$, the stagnation pressure, p_s, is found from Eqn. 2, and the the neutral gas density, n_g, from Eqn. 3. Equations 11 and 12 then enable T_w to be obtained, while the collisional power, P_{col}, is found using Eqn. 9. The electron temperature, T_e, is determined from Eqn. 13, and the electron density, n_e, from Eqn. 18. Once T_e and n_e are known, we can then calculate the different power terms with Eqns. 16-21. Similarly, Eqns. 27-29 yield the effective plasma resistance, r_p, from which the absorbed power, P_{abs}, and the total RF power, P_{rf}, can then be determined using Eqns. 23-24. Once all of the plasma/gas properties are known, the thruster performance is found from Eqns. 4-8.

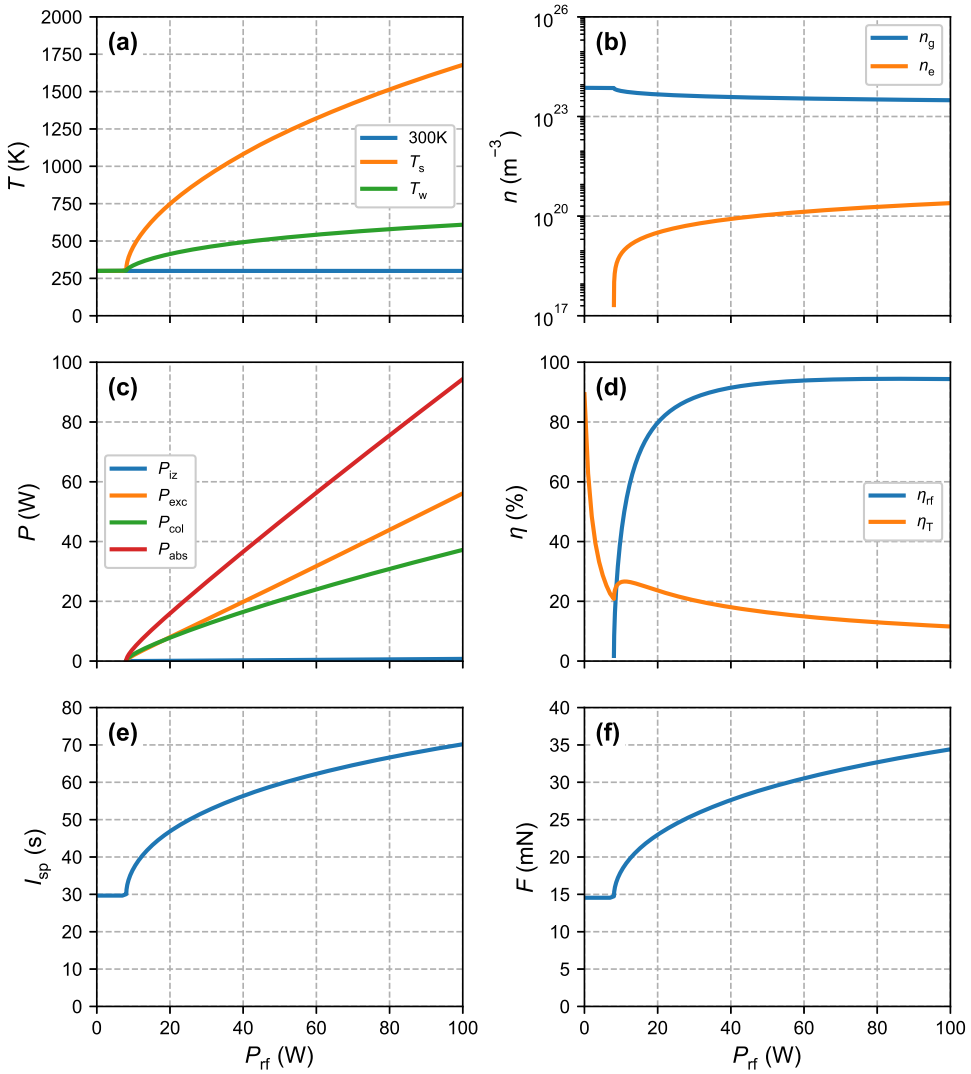


Fig. 5 Thruster properties and performance as a function of P_{rf} for $\dot{m} = 50$ mg/s, $R = 9.5$ mm, $L = 6.0$ cm, $f = 13.56$ MHz, and xenon propellant. **(a)** Stagnation and wall temperatures, **(b)** electron and neutral gas densities, **(c)** ionization, excitation, elastic scattering and total absorbed power, **(d)** RF and thruster efficiencies, **(e)** specific impulse, **(f)** thrust. Below about 8 W, no plasma can be sustained and so the system operates as a cold gas thruster.

Figure 5 shows properties and performance metrics of the thruster fueled with xenon for $\dot{m} = 50$ mg/s, and as a function of $P_{\mathrm{rf}} \in [0{,}100$ W]. Below a power of $P_{\mathrm{rf}} \approx 8$ W, a strong change in slope is seen for all results as a plasma cannot be sustained at these low power levels. Consequently, the system operates as a simple

cold gas thruster for $P_{\mathrm{rf}} < 8$ W, and all applied power is wasted as heat in the RF coil. As a constant mass flow rate is applied, the thruster performance therefore remains constant at these power levels: except for η_{T} which still accounts for the applied power to run the coil. For $P_{\mathrm{rf}} > 8$ W, a plasma is produced and both the electron density and gas temperature increase. This higher electron density also changes the electrical conductivity of the plasmas and reduces the electromagnetic skin depth, which leads to an increased plasma resistance, and hence a higher RF efficiency. Consequently, both the thrust and specific impulse increase, and in particular, more than double (for P_{rf} between 50-100 W) compared with the cold gas case.

As seen in Fig. 5 (c), the absorbed power is mainly distributed between P_{col} and P_{exc}. The model presented in Section 2 assumed electron impact excitation as an absolute energy loss. In reality however, excited atoms can de-excite via spontaneous radiative decay, releasing a photon in the process. Depending on the plasma conditions, this photon can either be lost to the boundaries or ambient environment (giving for example, a characteristic plume color), or can be re-absorbed by the plasma. Radiation trapping and reabsorption is a complex process that depends on the photon energy, the plasma properties, and the emission location. Indeed, the plasma is optically thin for some photon energies such that no reabsorption occurs, while the plasma is optically thick for other photon energies such that almost complete reabsorption takes place [12]. To avoid the need to include an explicit model resolving different excitation levels and radiation trapping, we introduce a radiation trapping coefficient, $\beta \in [0, 1]$ in Eq. 21.

$$\varepsilon_{\mathrm{c}} = \varepsilon_{\mathrm{iz}} + \beta \sum_{\mathrm{i}} \varepsilon_{\mathrm{exc,i}} \frac{K_{\mathrm{exc,i}}}{K_{\mathrm{iz}}} + \frac{3m}{M} k_{\mathrm{B}} (T_{\mathrm{e}} - T_{\mathrm{s}}) \frac{K_{\mathrm{el}}}{K_{\mathrm{iz}}} \tag{39}$$

For $\beta = 1$, the plasma is optically thin such that all radiation emission from spontaneous decay of excited states is permanently lost to the outside, while for $\beta = 0$, the plasma is optically thick such that all radiation is trapped and reabsorbed. As this energy is now retained within the plasma, various electron impact reactions, such as ionization, may be enhanced due to multi-step processes. The exact value of β is unknown and difficult to calculate. We therefore consider the two limiting cases, $\beta = 1$ and $\beta = 0$, below.

3.2 Fixed RF power

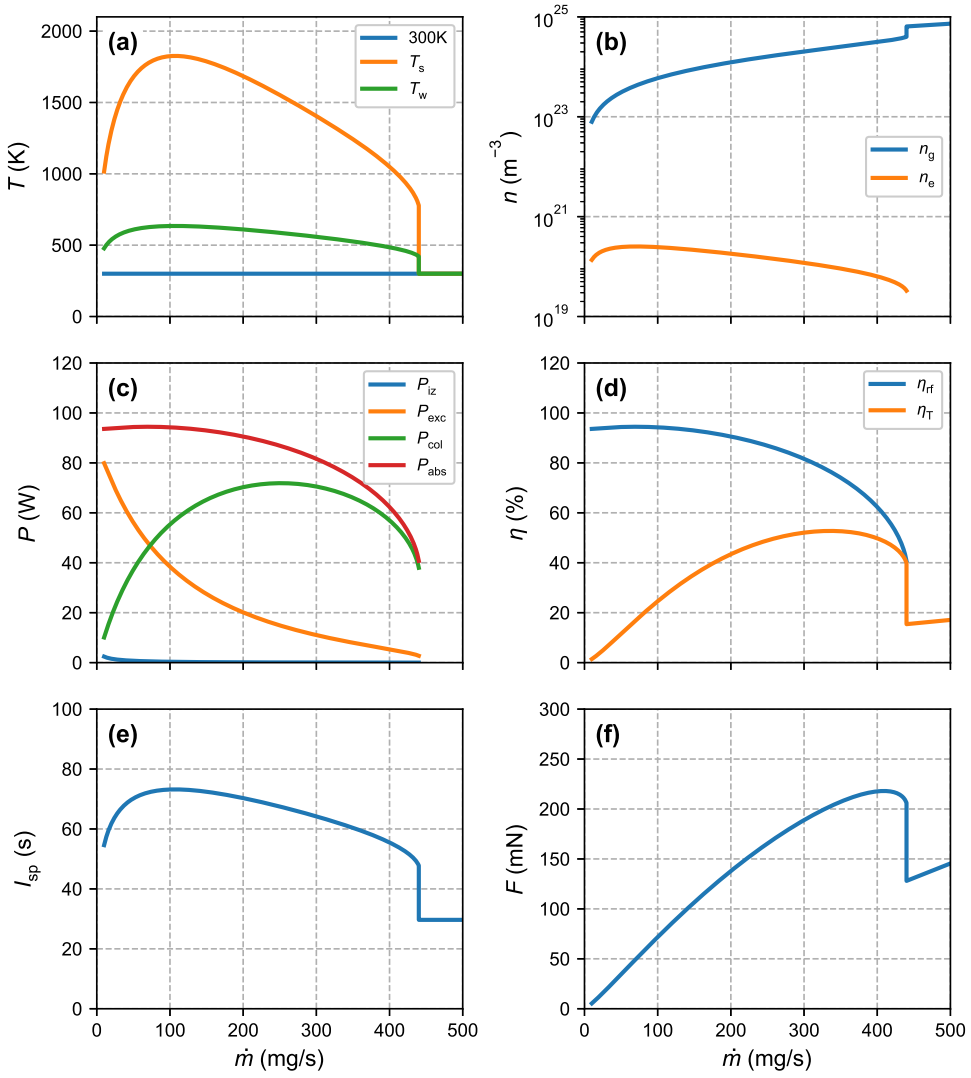


Fig. 6 Thruster properties and performance as a function of $\dot{m}$ for $P_{\mathrm{rf}} = 100$ W, $R = 9.5$ mm, $L = 6.0$ cm, $f = 13.56$ MHz, and xenon propellant. **(a)** Stagnation and wall temperatures, **(b)** electron and neutral gas densities, **(c)** ionization, excitation, elastic scattering and total absorbed power, **(d)** RF and thruster efficiencies, **(e)** specific impulse, **(f)** thrust.

Figure 6 shows properties and performance metrics of the thruster for $P_{\mathrm{rf}} = 100$ W, and as a function of $\dot{m}$. In contrast to Fig. 5, the cold gas case now occurs on the

right-hand side of the plots. Since the power is fixed, a plasma cannot be sustained at high mass flow rates. As the mass flow rate increases, T_s initially rapidly increases, but for $\dot{m} > 100$ mg/s, the gas temperature begins to decrease. Together with the increased mass flow rate, this raises the neutral gas density, which consequently lowers the electron temperature in order to satisfy ionization balance. Because of this, the collisional energy loss increases and so the electron density decreases. As a consequence, the plasma resistance goes down and, with it, the RF efficiency and absorbed power. Above a mass flow rate of 430 mg/s, the electron density becomes so low that coil-plasma power transfer is negligible and the plasma dies.

3.3 Comparison of propellants

Figures 5 and 6 were obtained using xenon propellant, and we now compare the thruster operation with krypton and argon. Figure 7 shows an example performance comparison of the different propellants as a function of $\dot{m}$ for $P_{rf} = 100$ W. As argon has a lower atomic mass, it enables a higher specific impulse than both krypton and xenon. However, an argon plasma is extinguished at a much lower mass flow rate. Consequently, krypton and xenon maintain a higher efficiency and can be operated over a wider range of operating conditions. Additionally, although argon gives a higher conventional specific impulse, this ignores propellant storage conditions and the tank mass. When factoring in such considerations, argon may be less attractive because for the same target mission total impulse, a larger and heavier propellant storage tank is needed. We can revisit the performance metrics to take this into account. Following Ref. [17], we extend the definition of the specific impulse (which is proportional to the total impulse per propellant mass), by introducing a new metric, the *effective specific impulse* $I_{sp,eff}$, proportional to the total impulse per propulsion system mass.

$$I_{sp,eff} = I_{sp} \frac{M_p}{M_{tot}} \tag{40}$$

This new metric now accounts for the dry mass of the propulsion system in addition to the propellant mass. Figure 7 compares the conventional and effective specific impulse for all three propellants. Compared to I_{sp}, $I_{sp,eff}$ effectively account for the different storage density of the propellants. This allows a more relevant comparison to be made to aid propellant selection. While argon has the highest I_{sp} because of its lower atomic mass, its low storage density results in a larger and heavier storage tank that increases the inert mass of the propulsion system. From this more global system perspective, xenon becomes the preferred propellant, followed by krypton. Figure 7 highlights how crucial the storage density of the propellant is. While Fig. 7 and the results above are for a fixed power, similar conclusions are obtained if the mass flow rate is instead fixed and the power varied.

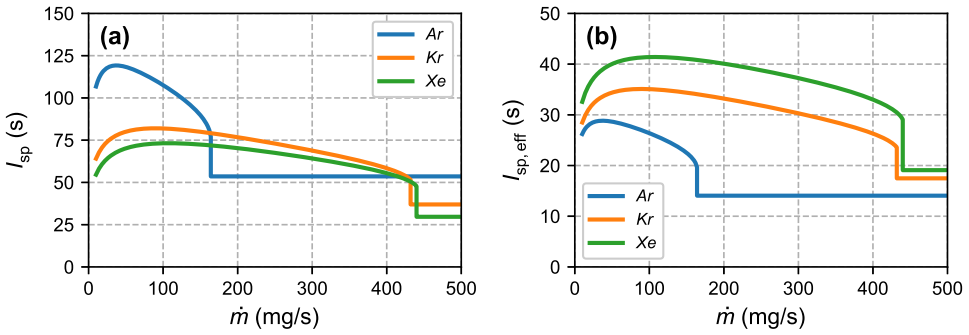


Fig. 7 Thruster performance as a function of $\dot{m}$ for different propellants and $P_{rf} = 100$ W, $R = 9.5$ mm, $L = 6.0$ cm, and $f = 13.56$ MHz. **(a)** specific impulse, **(b)** effective specific impulse.

3.4 Operating point and propellant selection

For a given thruster geometry (R and L) and frequency (f), Figs. 5 and 6 can be used to determine the optimal operating point depending on the chosen performance metric.

In this work, we fix the target total impulse I_T and the satellite power P_{sat}, and try to minimize the total mass of the system. Since $I_{sp,eff} = I_{sp}M_p/M_{tot} = I_T/(M_{tot}g_0)$, and as I_T is fixed here, maximizing $I_{sp,eff}$ will minimize M_{tot}. Hence, $I_{sp,eff}$ is our relevant performance metric. Fig. 7 enables us to compare propellants, and chose xenon, as it gives the highest effective specific impulse. According to Fig. 5 and 6, we must have the highest P_{rf} possible, and chose the corresponding $\dot{m}$ (for a fixed propellant, maximizing I_{sp} and $I_{sp,eff}$ are equivalent).

4 Geometry and frequency optimization

In this section, we now consider the thruster geometry (R and L) and RF frequency (f) as variables. The goal is to design a thruster with the lowest propulsion system mass such that the target total impulse of $I_T = 1$ kNs can be provided, while working with a fixed maximum input power of $P_{sat} = 100$ W from the satellite. This is equivalent to finding the thruster with the highest effective specific impulse.

Following the conclusions of the previous section, xenon is chosen as the preferred propellant. We will also choose the operating point by maximizing P_{rf} and selecting the optimal $\dot{m}$. To achieve this, the following optimization process is used:

1: The RF frequency, f, is initially fixed.
2: With this fixed frequency, we evaluate the maximum generator power output, P_{gen}, knowing the electrical DC-to-RF efficiency of the generator at this frequency.
3: We then initially assume perfect impedance matching such that $P_{rf} = P_{gen}$, and study the effect of different thruster geometries. For each thruster radius, R, and length, L, we consider the operating point that maximizes $I_{sp,eff}$ (as we work at fixed power, this is equivalent to choosing the mass flow rate that gives the optimal

effective specific impulse in Figs. 6 - 7). Among all considered geometries, we select that which gives the highest $I_{\mathrm{sp,eff}}$.

4: Using the plasma/gas properties of the selected thruster geometry (e.g n_{g}, n_{e}, T_{e}, etc.), we can then evaluate the plasma resistance r_{p} and reactance X_{d}. This gives us the required impedance matching network components, and its efficiency. From this, we can then evaluate $P_{\mathrm{rf}} = \eta_{\mathrm{IMN}} P_{\mathrm{gen}}$.

5: If required, we then re-iterate from Step 3 with the new power, P_{rf}, until convergence is obtained.

6: We now have the best thruster, and its properties, for a given frequency. We can then repeat the above steps for different frequencies and select the optimum.

4.1 Geometry maps

In this subsection, we proceed with Step 3 of the optimization process. We work with a fixed f and P_{rf}. For each geometry combination (i.e. R and L), we chose the mass flow rate that maximizes the effective specific impulse. The solution space is however restricted by adding several additional constraints. For example, given the available power level and small satellite mission scenario, the thruster size is expected to be limited. We therefore consider that the thruster chamber must fit within a single CubeSat unit (with standard dimensions of 10 cm $\times$10 cm $\times$10 cm), such that $L < 10$ cm. If we further assume that the thruster must not consume more than a quarter of a CubeSat unit volume, we have $R < 18$ mm. The latter value accounts for the RF coil diameter since $R_{\mathrm{c}} + R_{\mathrm{b}} = 2.5$ cm.

We also need to consider lower limits for R and L. The lower bound for the thruster chamber length is determined by the RF coil axial extent. To minimize the coil proximity effect, each coil spacing should be approximately $2R_{\mathrm{b}}$ apart [25]. Consequently, we have $L_{\mathrm{coil}} > 4NR_{\mathrm{b}} = 4.2$ mm, and taking $L/L_{\mathrm{coil}} = 0.9$ to accommodate edge effects while rounding up gives that $L > 5$ cm (for a 7-turn coil). A lower bound for R is more difficult to establish. We could imagine, for example, a reasonable manufacturing limit, and so here we select a representative limit requiring $R > 6$ mm. As we will see below however, the optimal thruster is not associated with such low values of R.

Another interesting geometrical constraint could be the volume of the propellant tank. It is reasonable to assume that only a certain number of CubeSat units can be allocated to the propellant. In what follows, we will implement a representative limit of $V_{\mathrm{tank}} < 750$ cm^3, which corresponds to three quarters of a CubeSat unit (while providing some margin).

We also need to check the temperature of the system so that the wall temperature does not exceed the material melting temperature. For this reason, any geometry where T_{w} approaches T_{melting} cannot be considered. Using alumina for the chamber walls [10], $T_{\mathrm{melting}} = 2372$ K. We then introduce a margin on this and only consider a thruster geometry to be feasible if the maximum wall temperature is less than 70% of this critical temperature: i.e. $T_{\mathrm{w,max}} < 1660$ K.

Another potential constraint is the stagnation pressure, where at least two limits need to be considered. Firstly, the dielectric chamber can only withstand a certain pressure, and may crack if the pressure is too high. The approximate maximum pressure is $p_{\mathrm{s}} < \frac{\sigma_{\mathrm{max}} d}{\alpha_{\mathrm{p}} R}$ with $\alpha_{\mathrm{p}} = 4$ a safety factor, and $\sigma_{\mathrm{max}} = 180$ MPa the maximum

tensile strength of alumina over the expected temperature range. For a large thruster radius (e.g. $R = 100$ mm), the mechanical pressure limit is approximately 12 bar. Additionally, the chamber stagnation pressure must be smaller than the pressure in the propellant tank, and small enough that a plasma can be sustained. For inductive plasma discharges, a reasonable upper pressure limit is about 1 bar, in order for the propellant to flow without difficulty through the system. Because this limit is lower than the strength limit, we take $p_\mathrm{s} < 1$ bar for the optimisation.

Table 4 summarizes the above constraints that are used in the optimization process, which now includes the following adjusted steps:

- For a fixed frequency and RF power, 2D maps (obtained by varying R and L) are obtained using the constraints in Tab. 4 and thruster properties are determined.
- We rule out all operating points where the imposed constraints on V_tank, T_w, and p_s are not respected.
- We optimize the performance metrics of interest with respect to R and L.

We note that the upper boundary on V_tank is not directly relevant for thruster optimization as we are already minimizing M_tot. Nonetheless, in the figures below, we keep this constraint to enhance the readability of the 2D maps.

Table 4 Constraint values applied during the optimization process.

	Lower limit	Upper limit
R	6 mm	18 mm
L	5 cm	10 cm
V_tank	-	750 cm^3
T_w	-	1660 K
p_s	-	1 bar

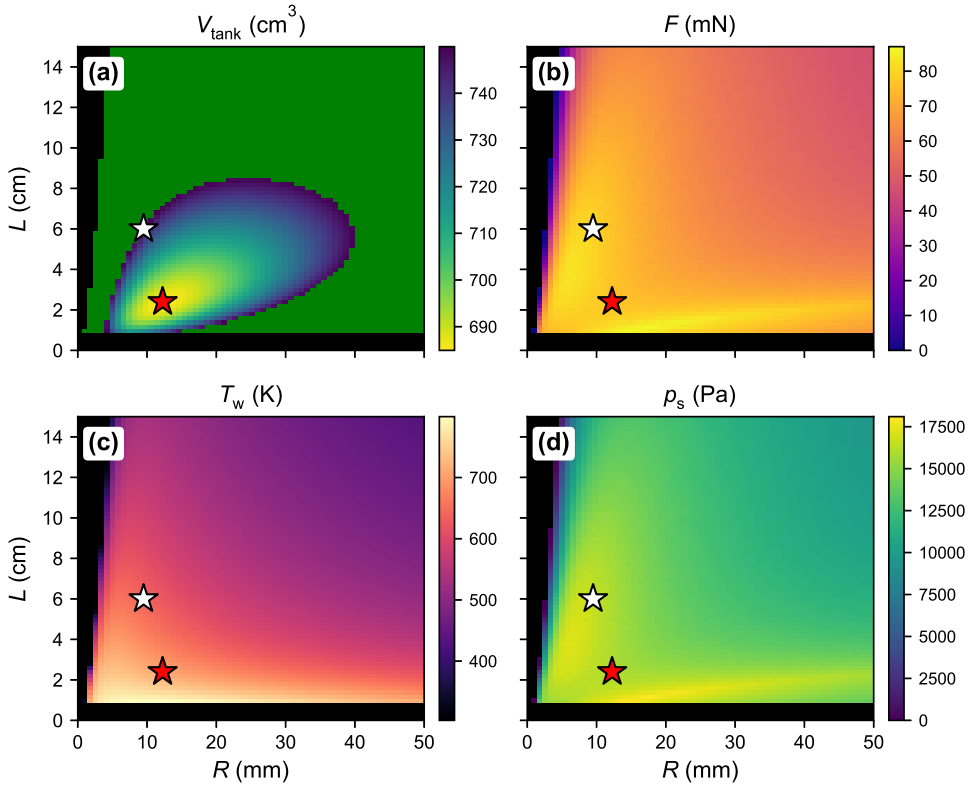


Fig. 8 Properties of a xenon-fueled thruster with respect to geometry. Here $f = 13.56$ MHz, $P_{\mathrm{rf}} = 100$ W, and $\beta = 1$. **(a)** Tank volume, **(b)** thrust, **(c)** wall temperature, and **(d)** stagnation pressure. The red star is the global minimum of V_{tank}, and the white star is the geometry used in Sec. 3.

Figure 8 shows 2D maps of the (R,L) space for $R \in [1, 50]$ mm and $L \in [1, 15]$ cm. The white star corresponds to the geometry previously used in Sec. 3, while the red star corresponds to the global optimum. We note that the global optimum falls outside of one of the lower boundary constraints (i.e. $L_{\mathrm{opti}} < 5$ cm), implying that the required thruster chamber is too small to adequately accommodate the RF coil. The green area in Fig. 8 (a) represents the volume constraint of 750 cm^3. Some larger chambers can reach a higher thrust, but require higher mass flow rates to achieve (at the expensive of a lower specific impulse), which results in more propellant needed for the mission.

The wall temperature is shown in Fig. 8 (c), where we see that the upper temperature limit of 1660 K is never reached. The maximum temperature is instead much lower and is between 700-800 K, which is similar to that observed in some other electric propulsion systems, such as Hall thrusters [26]. Although the wall temperature does tend to increase for very small R and/or L, the upper temperature limit is not

reached because the coil-plasma power transfer rapidly decreases, and thus the specified RF power of 100 W is not fully absorbed by the plasma. Indeed, for such extreme geometries, the coil-plasma coupling is so weak that most of the applied power is simply lost as heat in the coil itself (and which is assumed not to be conducted to the chamber walls). Regardless, even for the smallest possible geometry that satisfies all constraints (i.e. $R = 6$ mm and $L = 5$ cm), and assuming all input power is lost to the chamber walls, the estimated wall temperature is still only about 1030 K. Similarly, Fig. 8 (d) shows the thruster stagnation pressure, where it is seen that the maximum pressure is just above 20 kPa, which is far from the constraint pressure of 1 bar.

Finally, the black area on the left of all subplots corresponds to the geometries where a plasma cannot be sustained. As the thruster performance in this region is extremely poor (corresponding to a cold gas thruster), these conditions are not considered further.

4.2 Impedance matching network

Once the optimal geometry and operating conditions are known, the plasma resistance and reactance can be evaluated and the required impedance matching network components determined. Depending on the plasma properties, either a "double C type" or an "L+C type" matching network is needed.

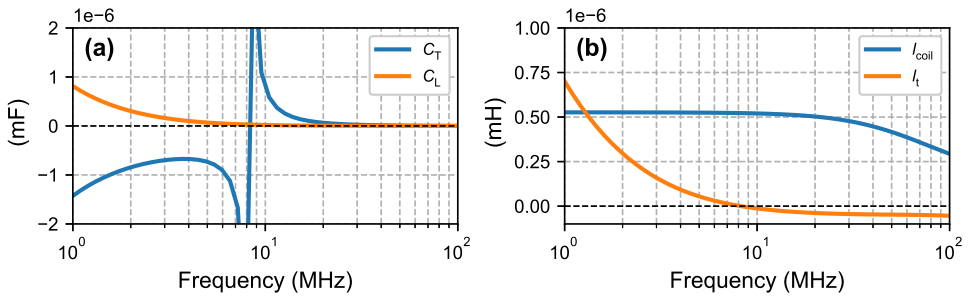


Fig. 9 Required impedance matching network component values with respect to frequency for example plasma/gas parameters of $n_g = 4 \times 10^{23}$ m^{-3}, $n_e = 2 \times 10^{20}$ m^{-3}, and $T_e = 0.61$ eV. Here **(a)** correspond to "double C type" network, and **(b)** an "L+C type" network.

To better understand the dependency of impedance matching network components, Fig. 9 shows the required component values as a function of RF frequency, for fixed plasma properties. Here, l_{coil} is the inductance of the RF coil as a reference for $R = 10$ mm and $L = 3$ cm.

Fig. 9 shows that above about 8 MHz, a "double C type" matching network is needed, while for frequencies below this, a "L+C type" is needed. As the resistance of the matching inductor in this case is not negligible, the matching, while ideal, is not optimal as there are additional power losses in the matching inductor. By contrast,

both matching and power transfer is optimal for the "double C" type as the internal resistance of many capacitors is negligible.

Not only does the chosen frequency change the needed IMN, but also the plasma parameters (i.e. n_g, n_e, T_e) also need to be taken into account. For a fixed frequency, a change in plasma properties necessitates a transition from a "double C" type to a "L+C type" type IMN. This dependency on the plasma parameters is one reason why an iterative process is needed for the optimization.

4.3 Full optimization ($\beta = 1$)

With the global optimization process (varying R, L, and f) introduced in the subsections above, we now perform a full optimization for the limiting case $\beta = 1$, which corresponds to an optically thin plasma where all excitation energy is lost. Figure 10 shows a cropped version of Fig. 8 accounting for the lower and upper boundary constraints (giving $R \in [6, 18]$ mm and $L \in [5, 10]$ cm). The red star indicates the optimum within these boundaries, which is located near the bottom right corner of the map.

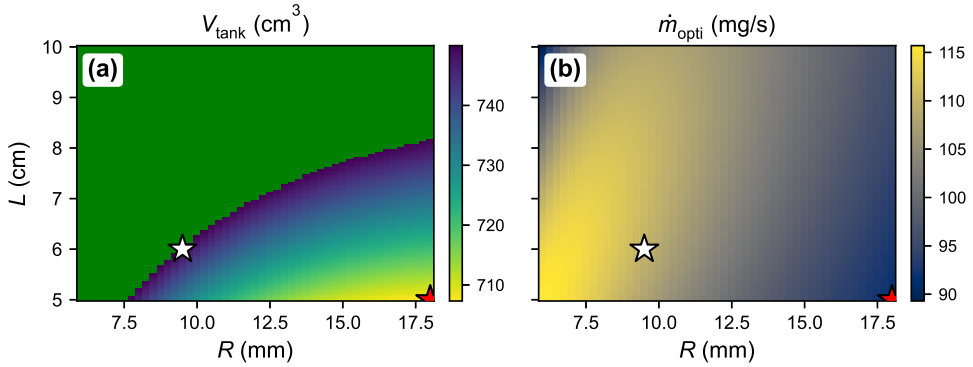


Fig. 10 Properties of a xenon-fueled thruster with respect to geometry and accounting for the constraints in Tab. 4. Here, $f = 13.56$ MHz, $P_{rf} = 100$ W, and $\beta = 1$. **(a)** V_{tank} (cm^3), and **(b)** $\dot{m}_{opti}$ (mg/s).

The same process can then be repeated for different frequencies to find the overall optimal combination of R, L, and f. Table 5 summarizes the properties of the optimal thruster found, while Fig. 11 shows the component values required by the impedance matching network. For $f > 1$ MHz, a "double C type" matching network is needed.

Table 5 Optimized thruster for $\beta = 1$ and $f = 2$ MHz.

Symbol	Value	Symbol	Value
R	18 mm	n_g	4.50×10^{23} m^{-3}
L	5 cm	n_e	1.22×10^{20} m^{-3}
f	2 MHz	T_e	0.60 eV
IMN	"double C type"	η_{rf}	94.68 %
η_{IMN}	100 %	$\dot{m}_{opti}$	78 mg/s
C_L	7 nF	F	57.46 mN
C_T	52 nF	M_{tot}	2.59 kg
		V_{tank}	735 cm^3

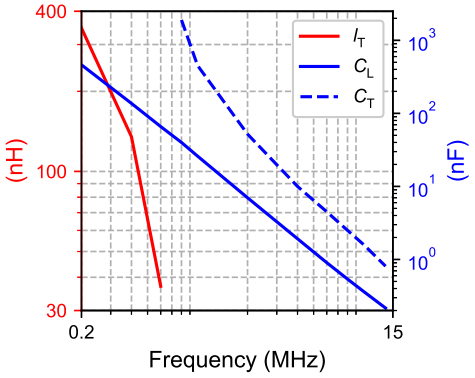


Fig. 11 Required impedance matching network components with respect to frequency for an optimized thruster with $P_{sat} = 100$ W and $\beta = 1$. The solid and dashed blue curves correspond to a "double C type" network, while the solid blue and red curves correspond to an "L+C type" network.

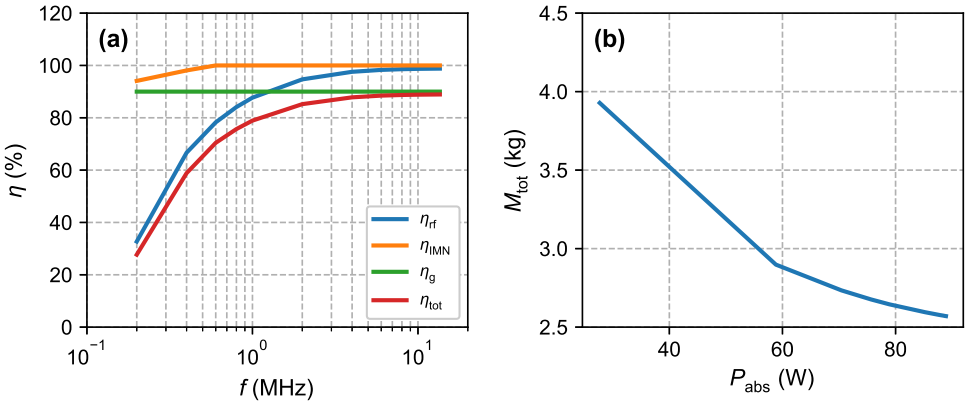


Fig. 12 **(a)** System and total efficiencies, and **(b)** total propulsion system mass for an optimized xenon-fueled thruster. Here, $P_{sat} = 100$ W and $\beta = 1$.

Figure 12 (a) shows the various system efficiencies as a function of frequency, while η_{tot} is the total efficiency. The optimal thruster frequency occurs when this total efficiency is maximized. The impedance matching network efficiency is very high and close to 100%, except for $f < 0.6$ MHz. The main power loss factor corresponds to the coil-plasma power transfer efficiency η_{rf}. While η_{rf} is a consequence of the optimization process, $\eta_{\text{g}} = 90\%$ is only a representative inference. A more advanced generator electrical model, or an empirical model based on experimental measurements, is required to describe this further. Typically though, this efficiency decreases as the frequency increases [4]. With real experimental data for $\eta_{\text{g}}(f)$, we would likely observe the total efficiency to achieve a maximum between 1 and 5 MHz.

Finally, Fig. 12 (b) shows the optimal propulsion system mass with respect to absorbed power (i.e. the total efficiency). We can see that the total mass decreases with the absorbed power. Thus, the optimal frequency is the frequency that maximizes $\eta_{\text{tot}} \propto P_{\text{abs}}$.

4.4 Full optimization ($\beta = 0$)

We now consider the opposite limiting case of $\beta = 0$, which corresponds to an optically thick plasma where complete radiation trapping occurs. In this case, the power absorbed by the plasma is only distributed between elastic scattering, ionization, and kinetic energy losses to the walls, which changes the behavior of the thruster. Figure 13 shows the corresponding 2D maps, where the optimum is now different than the optimum of the previous case. For all geometries, Fig. 13 shows that radiation trapping leads to a lower tank volume than Fig. 10, and hence a reduced propellant mass. This is a result of the lower overall system power loss, which implies a higher gas temperature, and hence specific impulse.

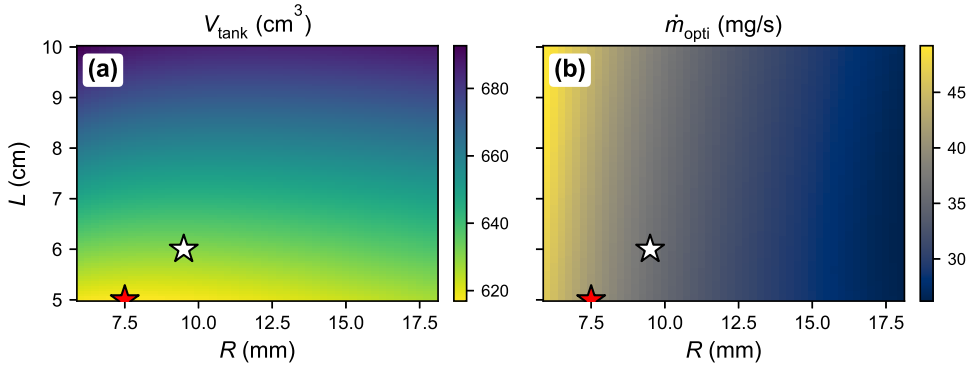


Fig. 13 Properties of a xenon-fueled thruster with respect to geometry and accounting for the constraints in Tab. 4. Here, $f = 13.56$ MHz, $P_{\text{rf}} = 100$ W, and $\beta = 0$. **(a)** V_{tank} (cm^3), and **(b)** $\dot{m}_{\text{opti}}$ (mg/s).

Table 6 Optimized thruster for $\beta = 0$ and $f = 2$ MHz.

Symbol	Value	Symbol	Value
R	9.25 mm	n_g	1.63×10^{23} m^{-3}
L	5 cm	n_e	1.15×10^{21} m^{-3}
f	2 MHz	T_e	0.70 eV
IMN	"L+C type"	η_rf	92.67 %
η_IMN	98.87 %	$\dot{m}_\mathrm{opti}$	33 mg/s
C_L	10 nF	F	28.44 mN
l_T	470 nH	M_tot	2.29 kg
		V_tank	629 cm^3

The same optimization process can again be repeated for different frequencies, and the overall optimal thruster properties are summarized in Tab. 6. As the effective power loss is lower with radiation trapping, the optimal thruster is better than that for the $\beta = 1$ case. We also note that an "L+C type" impedance matching network so now needed for all frequencies. Figure 14 shows the l_T and C_L values needed for the impedance matching network as a function of frequency. At lower frequencies, the required inductance is higher, which then increases power losses in the impedance matching network because of the higher corresponding inductor resistance. This can also be more clearly seen in Fig. 15, which shows the various system efficiencies and the total propulsion system mass.

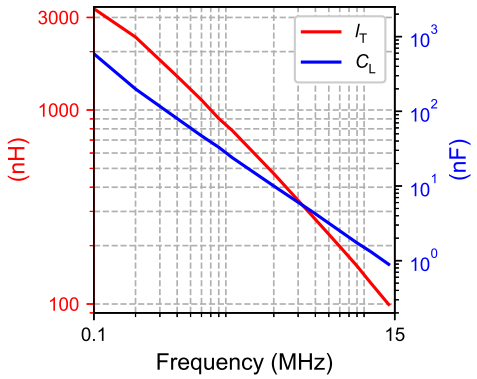


Fig. 14 Required impedance matching network components with respect to frequency for an optimized thruster with $P_\mathrm{sat} = 100$ W and $\beta = 0$. The solid blue and red curves correspond to an "L+C type" network.

Type	Elec-Power	Thrust	I_{sp}	Total Impulse	Dry Mass	Total Mass
Hall-effect[27]	60 W	1.8 mN	800 s	5 kNs	2.3 kg	2.43 kg
Helicon[28]	500 W	7 mN	400 s	-	5.9 kg	-
FEEP[29]	45 W	350 μN	4500 s	4 kNs	1.28 kg	1.5 kg
Ion-gridded[30]	75 W	1.1 mN	2150 s	3.2 kNs	1.4 kg	2.9 kg
MET[31]	100 W	4.5 mN	180 s	7 kNs	1.5 kg	2.5 kg
ICP	100W	60 mN	76 s	1 kNs	0.5 kg	2.6 kg

Table 7 Comparison of different electric propulsion systems.

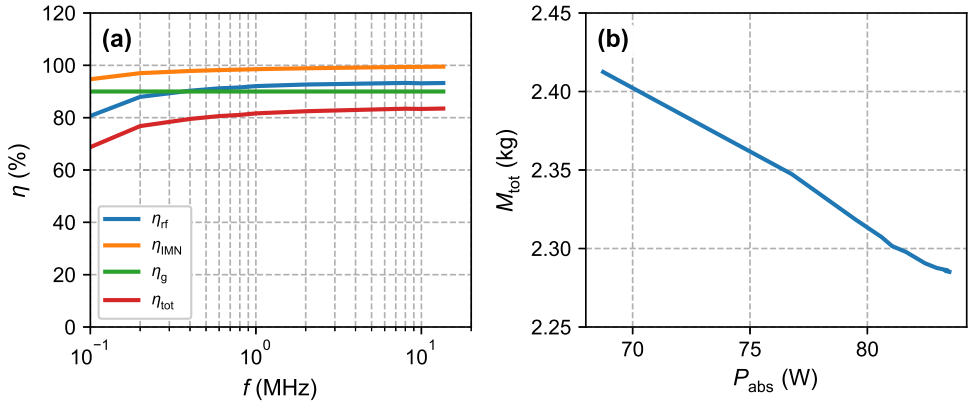


Fig. 15 **(a)** System and total efficiencies, and **(b)** total propulsion system mass for an optimized xenon-fueled thruster. Here, $P_{sat} = 100$ W and $\beta = 0$.

Figures 12 and 15 show that P_{abs} (via the coil-plasma power transfer efficiency, η_{rf}) is the key power parameter influencing performance. Aside from varying the thruster geometry, frequency, and plasma properties, the power transfer efficiency may also be modified by varying the coil properties, such as the number of turns. Although the plasma resistance in the present model is independent of the number of turns, fewer turns are expected to result in a more non-uniform electromagnetic field and stronger edge effects. Thus, reducing the number of turns may decrease the overall power transfer efficiency (leading to worse performance), but allow the thruster chamber length to be decreased (potentially leading to better performance). Finally, we note that while the $\beta = 0$ case gives better performance than the $\beta = 1$ case, in reality complete radiation trapping does not occur, such that the optimal thruster is expected to lie somewhere between the optimal thrusters for both of these limiting cases.

5 Conclusion

For a target total impulse of 1 kNs, and an available satellite power of 100 W, we have optimized an RF ICP electrothermal plasma thruster to obtain a propulsion system with the lowest total mass. For the propellants considered, xenon gives the best

performance, largely because of its high atomic mass and storage density. Through the optimization process, we then found the required RF frequency, thruster chamber dimensions, operating conditions (i.e. mass flow rate and power), and required impedance matching network design. While the present study could be extended to other interesting propellants (such as water or ammonia), such molecular substances have a much more complex plasma chemistry. In addition, collisional power losses are significantly higher, and for liquid propellants, further power is needed for vaporization. Indeed, previous related studies have shown that xenon and krypton, while maybe not yielding the highest specific impulse (or even effective specific impulse), are expected to give the highest thrust-to-power ratio [17].

We can compare the results of the present optimization study for RF ICP thrusters with other existing electric propulsion systems, as shown in Tab. 7, for various performance metrics. To be conservative, we have used the optimized thruster for $\beta = 1$, while data for the other electric propulsion systems is taken from available datasheets. Here, we have chosen systems with a similar order of magnitude power level for a more balanced comparison. All system also have a similar total mass. A clear disadvantage of RF ICP thrusters, particularly when using a heavy propellant like xenon, is the relatively low specific impulse. This is however compensated for by the much higher thrust level that can be achieved. Consequently, orbital maneuvers can be performed much faster, and the propulsion system may also be useful for close proximity operations [11]. Another important advantage is the lack of an electron-emitting neutralizer, and the need for only a single power supply (to operate the RF generator). For larger satellites and/or more complex missions, there is also another important advantage. Since high-performance electric propulsion systems like gridded ion or Hall thrusters currently use xenon or krypton, an RF ICP thruster could share the same propellant tank, enabling multi-mode propulsion operation [32]. That is to say, a high specific impulse mode would make use of the gridded ion or Hall thruster, while a high thrust mode would make use of the RF ICP thruster. A similar approach as been used previously on the PROCYON satellite where multi-mode operation between a gridded ion thruster and a cold gas thruster was employed [33].

Finally, we address several ways of expanding or improving the present work. Firstly, the model can be enhanced. For example, experimental data can help to better inform some of the parameters or scaling laws, such as the variation of generator DC-to-RF conversion efficiency with frequency. Similarly, the formulation for $P_{\mathrm{w,cond}}$ (given by Eqn. 10) is only a type of ansatz, while the formulae for r_{coil} and r_{IMN} are simplified, and do not explicitly account for key aspects such as the proximity effect. Moreover, some parameters used here, such as β, are not known and so we have considered only the upper and lower limiting cases. Finally, the optimization algorithm could be extended to include additional variables, such as the number of coil turns, and could potentially be incorporated into a machine learning model (such as has been done for other electric propulsion systems such as Hall thrusters [34]). Since the thruster model developed here is completely analytically, a large amount of training data be generated very quickly. Having such a machine learning model would then more effectively aid practical thruster design, particularly if modified or additional parameter constraints are required.

Declarations

Funding: L.A. would like to thank the *Académie Spatiale d'Île de France* and *Ecole Polytechnique* for providing funding to travel to Australia to perform this work.
Competing interests: The authors declare no competing interests.
Data availability: The data that support the findings of this study are available from the corresponding author upon reasonable request.
Authors' contributions: L.A. developed the model, performed the analysis, and wrote the original draft of the manuscript. T.L. contributed to the interpretation of the results, reviewed and revised the manuscript, and supervised the work.

Appendix A Reaction rates

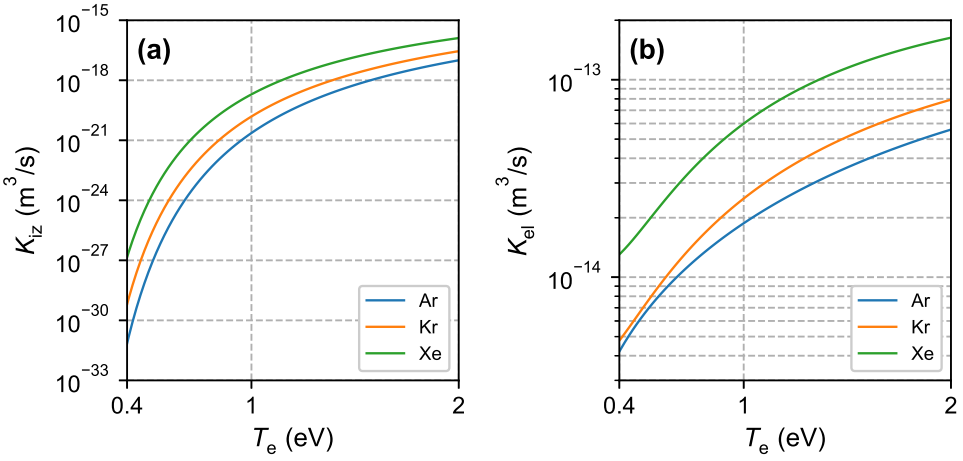


Fig. A1 Ionization and elastic scattering rate coefficients for argon, krypton, and xenon as a function of electron temperature.

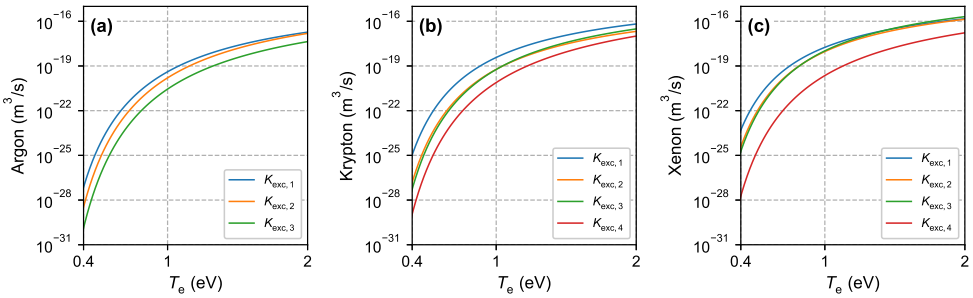


Fig. A2 Lumped excitation rate coefficients for argon, krypton, and xenon as a function of electron temperature.

Figures A1 and A2 show the ionization, excitation, and elastic scattering rate coefficients for argon, krypton, and xenon as a function of electron temperature as used in this work. Rate coefficients are computed from Eqn. 22 using cross-section data from the LXCat database [24].

As the model code relies on many calls to the rate coefficient functions, calculating these rate coefficients from Eqn. 22 at each iteration would unnecessarily increase computing time. Therefore, the rate coefficients in Figs. A1 and A2 are fitted to an Arrhenius-type function (for ionization and excitation), or a polynomial function (for elastic scattering):

$$K_\mathrm{x}(T_e) = A T_\mathrm{e}^B \exp\left(-\frac{C}{T_\mathrm{e}}\right) \tag{A1}$$

$$K_\mathrm{el}(T_\mathrm{e}) = \sum_{\mathrm{i}=0}^{n} c_\mathrm{i} T_\mathrm{e}^\mathrm{i} \tag{A2}$$

where $A, B, C, c_\mathrm{i} \in \mathbb{R}$ are evaluated for K_x in units of m^3/s and T_e in eV. The result of the fitting is given in Tab. A1.

The fit was performed with 100 points evenly distributed for $T_\mathrm{e} \in [0.1, 2]$ using the function `curve_fit` in `scipy.optimize`. The Arrhenius-type fit was performed on the logarithm of the data.

Table A1 Fitting coefficients for different propellants and collisional reaction processes.

Argon					K_{el}	$n = 3$
	A	B	C	R^2	c_0	$-2.10700986 \times 10^{-15}$
K_{iz}	1.54×10^{-14}	0.73	15.70	1.00000	c_1	$1.52246497 \times 10^{-14}$
$K_{\mathrm{exc},1}$	4.32×10^{-15}	0.52	11.58	1.00000	c_2	$6.26359850 \times 10^{-15}$
$K_{\mathrm{exc},2}$	7.13×10^{-15}	0.52	13.00	1.00000	c_3	$-6.05704294 \times 10^{-16}$
$K_{\mathrm{exc},3}$	3.35×10^{-15}	0.51	14.00	1.00000	R^2	1.00000

Krypton					K_{el}	$n = 3$
	A	B	C	R^2	c_0	$-1.02384051 \times 10^{-14}$
K_{iz}	1.76×10^{-14}	0.77	13.94	1.00000	c_1	$4.77595775 \times 10^{-14}$
$K_{\mathrm{exc},1}$	7.30×10^{-15}	0.30	9.87	1.00000	c_2	$-1.75786289 \times 10^{-14}$
$K_{\mathrm{exc},2}$	5.40×10^{-15}	0.30	11.44	1.00000	c_3	$4.95555325 \times 10^{-15}$
$K_{\mathrm{exc},3}$	1.03×10^{-14}	0.37	12.10	1.00000	R^2	0.99998
$K_{\mathrm{exc},4}$	2.75×10^{-15}	1.20	12.80	1.00000		

Xenon					K_{el}	$n = 4$
	A	B	C	R^2	c_0	$8.06130919 \times 10^{-15}$
K_{iz}	3.56×10^{-14}	0.63	12.10	1.00000	c_1	$-6.64693700 \times 10^{-14}$
$K_{\mathrm{exc},1}$	6.87×10^{-15}	0.43	8.26	1.00000	c_2	$1.74263472 \times 10^{-13}$
$K_{\mathrm{exc},2}$	1.19×10^{-14}	0.46	9.50	1.00000	c_3	$-7.53156552 \times 10^{-14}$
$K_{\mathrm{exc},3}$	2.40×10^{-14}	0.43	10.07	1.00000	c_4	$1.92707330 \times 10^{-14}$
$K_{\mathrm{exc},4}$	2.73×10^{-15}	1.13	11.71	1.00000	R^2	0.99994

Appendix B Thermal conductivity

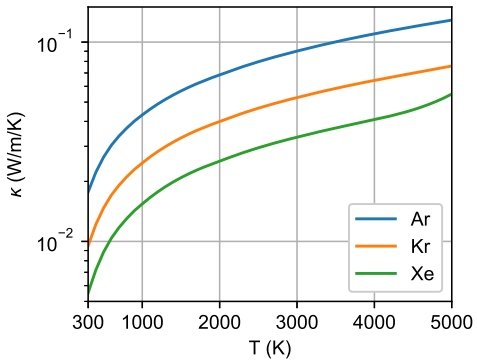


Fig. B3 Thermal conductivity of argon, krypton, and xenon as a function of temperature.

Figure B3 shows the thermal conductivity of argon, krypton, and xenon with respect to the gas temperature. Data is taken from the NIST database [35]. For the model, evenly distributed points for $T \in [300\ \mathrm{K}, 15000\ \mathrm{K}]$ are taken with a step of 100 K, and

using a cubic interpolation for points in between. For the latter, we used `interp1d` from the library `scipy.interpolate`.

References

[1] Simon, M.A., Knowles, S.C., Curran, F.M., Hardy, T.L.: Low power arcjet life issues. In: 19th International Electric Propulsion Conference (1987). https://ntrs.nasa.gov/citations/19870052361

[2] Nakagawa, T., Ohtsuka, H.: Thermal design and experimental verification of a three-dimensional-printed resistojet. Journal of Propulsion and Power **38**(1), 120–130 (2021) https://doi.org/10.2514/1.B38187

[3] Kline, J.L., Micci, M.M.: Microwave electrothermal thruster performance in helium and nitrogen. Journal of Propulsion and Power **15**(6), 844–849 (1999) https://doi.org/10.2514/2.5513

[4] Xie, T.: Design and development of the class e RF power amplifier prototype by using a power MOSFET. Technical Report CRESIS TR 129, Center for Remote Sensing of Ice Sheets (CReSIS), University of Kansas, Lawrence, KS (July 2007)

[5] Biswas, S.: An investigation of plasma dynamics within microwave electrothermal thruster cavities. Dissertation, The Pennsylvania State University (2023). https://etda.libraries.psu.edu/files/final_submissions/1358

[6] Foust, J.: Momentus tug raises orbit with water-fueled thruster. SpaceNews. Accessed: 2026-08-20 (2023). https://spacenews.com/momentus-tug-raises-orbit-with-water-fueled-thruster/

[7] Micci, M.M.: Encyclopedia of Aerospace Engineering. John Wiley & Sons, Chichester, UK (2010)

[8] Pollard, J., Lichtin, D., Cohen, R.: RF discharge electrothermal propulsion results from a lab-scale thruster. In: 23rd Joint Propulsion Conference. American Institute of Aeronautics and Astronautics, San Diego, CA, USA (1987). Paper AIAA-1987-2124

[9] Fujino, T., Yamauchi, M.: Numerical study of plasma-fluid characteristics and thrust performance of a low-power argon inductively coupled plasma electrothermal thruster. Journal of Applied Physics **128**(17), 173302 (2020) https://doi.org/10.1063/5.0022018 https://pubs.aip.org/aip/jap/article-pdf/doi/10.1063/5.0022018/19753240/173302_1_online.pdf

[10] Lafleur, T., Corr, C.S.: Characterization of a radio-frequency inductively coupled electrothermal plasma thruster. Journal of Applied Physics **130**(4), 043304 (2021) https://doi.org/10.1063/5.0056124 https://pubs.aip.org/aip/jap/article-pdf/doi/10.1063/5.0056124/15264219/043304_1_online.pdf

[11] Sadler, G., Saridede, E., Lucca Fabris, A.: Numerical and experimental analysis of a radiofrequency inductively coupled electrothermal thruster. In: 39th International Electric Propulsion Conference (IEPC), London, United Kingdom (2025). Paper IEPC-2025-375

[12] Ait Ammar, Y., Pascale, A., Corr, C.S., Lafleur, T.: Collisional-radiative model of a supersonic inductive plasma torch. Plasma Sources Science and Technology **34**(10), 105001 (2025)

[13] Lieberman, M.A., Lichtenberg, A.J.: Principles of Plasma Discharges and Materials Processing, 2nd edn. John Wiley & Sons, Hoboken, New Jersey (2005)

[14] Sharma, A., Kimball, J.W.: Hybrid model to evaluate the frequency-dependent leakage inductance of partially-filled transformers. Power Electronic Devices and Components **5**, 100038 (2023) https://doi.org/10.1016/j.pedc.2023.100038

[15] Pozar, D.M.: Microwave Engineering, 4th edn. John Wiley & Sons, Hoboken, NJ (2011)

[16] Tsay, M., Model, J., Barcroft, C., Frongillo, J., Zwahlen, J., Fend, C.: Integrated testing of iodine BIT-3 rf ion propulsion system for 6U CubeSat applications. In: 35th International Electric Propulsion Conference, Atlanta, Georgia (2017). Electric Rocket Propulsion Society. Paper IEPC-2017-264

[17] Martínez Martínez, J., Lafleur, T.: On the selection of propellants for cold/warm gas propulsion systems. Acta Astronautica **212**, 54–69 (2023) https://doi.org/10.1016/j.actaastro.2023.07.031

[18] Humble, R.W., Henry, G.N., Larson, W.J.: Space Propulsion Analysis and Design. Space Technology Series. McGraw-Hill Companies, New York, NY (1995)

[19] Huzel, D.K., Huang, D.H.: Modern Engineering for Design of Liquid-Propellant Rocket Engines. Progress in Astronautics and Aeronautics, vol. 147. American Institute of Aeronautics and Astronautics, Washington, D.C. (1992). Based on the original NASA SP-125 (1971)

[20] Sutton, G.P., Biblarz, O.: Rocket Propulsion Elements, 9th edn. John Wiley & Sons, Hoboken, New Jersey (2016)

[21] Henry, G.N., Larson, W.J., Humble, R.W.: Space Propulsion Analysis and Design. McGraw-Hill, New York, NY (1995)

[22] Wertz, J.R., Everett, D.F., Puschell, J.J.: Space Mission Engineering: The New SMAD. Microcosm Press, Hawthorne, CA (2011)

[23] Martínez, J.M., Murphy, A.B., Lafleur, T.: Investigation of propellants for electrothermal propulsion systems: Application to radio-frequency inductively

coupled plasma thrusters. Journal of Applied Physics **139**(3) (2026)

[24] LXCat Team: LXCat: an open-access, web-based platform for data needed for modeling low temperature plasmas. http://www.lxcat.net. Data extracted in April 2026

[25] Medhurst, R.G.: H.f. resistance and self-capacitance of single-layer solenoids. Wireless Engineer **24**, 35–43 (1947)

[26] Martinez, R.A., Dao, H., Walker, M.L.R.: Power deposition into the discharge channel of a hall effect thruster. Journal of Propulsion and Power **30**(1), 209–220 (2014) https://doi.org/10.2514/1.B34897

[27] Exotrail: ExoMG™- Nano Product Specifications. (2022). Exotrail. Fiche technique commerciale du propulseur à effet Hall ExoMG-Nano. https://www.exotrail.com

[28] Phase Four, Inc.: Maxwell Block 1 Engine - Technical Datasheet. (2021). Phase Four, Inc.. Fiche technique officielle du propulseur Helicon Maxwell B1. https://www.phasefour.io

[29] Enpulsion GmbH: ENPULSION NANO Thruster Datasheet. (2021). Enpulsion GmbH. Spécifications commerciales du propulseur FEEP à Indium liquide (gamme Nano/Lark). https://www.enpulsion.com

[30] Busek Co. Inc.: BIT-3 RF Ion Thruster Datasheet. (2016). Busek Co. Inc.. Fiche technique officielle du propulseur ionique à grilles BIT-3. http://www.busek.com/index_htm_files/70010819C.pdf

[31] Farahani, L., Micci, M.M.: Performance of a water microwave electrothermal thruster. In: 48th AIAA/ASME/SAE/ASEE Joint Propulsion Conference & Exhibit (2012). https://doi.org/10.2514/6.2012-3843

[32] Rovey, J.L., Lyne, C.T., Mundahl, A.J., Rasmont, N., Glascock, M.S., Wainwright, M.J., Berg, S.P.: Review of multimode space propulsion. Progress in Aerospace Sciences **118**, 100627 (2020) https://doi.org/10.1016/j.paerosci.2020.100627

[33] eoPortal: PROCYON (Proximate Object Close Flyby with Optical Navigation). Accessed: 2026-09-01 (2014). https://www.eoportal.org/satellite-missions/procyon#eop-quick-facts-section

[34] Marianacci, A., Mazouffre, S.: Supervised machine learning-based hall thruster scaling. Journal of Electric Propulsion **3**, 14 (2024) https://doi.org/10.1007/s44205-024-00077-y

[35] National Institute of Standards and Technology: NIST Chemistry WebBook, NIST Standard Reference Database Number 69. NIST. Accessed: 2026-06-17.

https://webbook.nist.gov